Chemical Science

ROYAL SOCIETY OF CHEMISTRY

EDGE ARTICLE

View Article Online
View Journal

Check for updates

Cite this: DOI: 10.1039/d5sc08926c

All publication charges for this article have been paid for by the Royal Society of Chemistry

Received 15th November 2025
Accepted 22nd December 2025

DOI: 10.1039/d5sc08926c

rsc.li/chemical-science

# Highly efficient $CO_2$ hydrogenation to long-chain linear α-olefins *via* CO intermediate enrichment over Na/FeMn/$ZrO_2$ catalysts

Kangzhou Wang, *[a] Tong Liu,[b] Pengqi Hai,[a] Shunnosuke Fujii,[c] Chufeng Liu,[c] Hanyao Song,[c] Caixia Zhu,[d] Guangbo Liu,[de] Jianli Zhang, *[b] Zhou-jun Wang *[bf] and Noritatsu Tsubaki *[c]

Although significant progress has been made in the oriented conversion of $CO_2$ to long-chain linear α-olefins (LAOs), cooperatively regulating C–O bond activation and C–C coupling *via* tailored catalyst microstructures remains a persistent challenge. Herein, a highly efficient Na/FeMn/$ZrO_2$ catalyst has been fabricated through a covalent anchoring strategy, which achieves a LAOs/$C_{4+}$ selectivity of 68% and an O/P ratio of 5.1 in $CO_2$ hydrogenation to LAOs. There is a pronounced interaction between Fe species and $MnCO_3$ in Na/FeMn/$ZrO_2$ catalysts, which promotes the formation and stabilization of iron carbides. Meanwhile, $Fe_5C_2$–$ZrO_2$ interfaces possess strong adsorption capacity for CO intermediates, resulting in the accumulation of generated CO on the $Fe_5C_2$ active sites. The higher CO concentration on the $Fe_5C_2$–$ZrO_2$ interface is beneficial to the C–C coupling reaction, thereby significantly improving the production of high-value olefins. These results will provide a theoretical basis and guidance for developing efficient catalysts for the oriented conversion of $CO_2$ to LAOs.

## Introduction

With rapid economic development, fossil energy consumption continues to rise, emitting substantial anthropogenic carbon dioxide ($CO_2$) into the environment and causing serious environmental consequences.[1–5] Directly converting $CO_2$ into chemicals *via* integration with green hydrogen technology not only reduces overdependence on fossil fuels and alleviates $CO_2$-induced environmental problems, but also provides an effective strategy for $CO_2$ resource utilization and high value-added chemical production.[6–9] $CO_2$ hydrogenation can produce CO,[10] light olefins,[11,12] gasoline,[13] methanol,[14] jet fuels,[15] and long-chain linear α-olefins.[16] Among these products, long chain linear α-olefins (LAOs, $C_{4+}^{=}$ a terminal carbon–carbon double bond) are important chemical intermediates that are used in synthetic lubricants, new polymers, high-octane gasoline, corrosion inhibitors, and agricultural chemicals.[17–19] Currently, LAOs are mostly generated by thermal cracking of petroleum resources. Therefore, the oriented conversion of $CO_2$ coupled with green hydrogen to LAOs is important for the sustainable development of feedstocks.

$CO_2$ hydrogenation to LAOs mainly involves the reverse water–gas shift (RWGS) reaction and C–C coupling reaction. In this process, $CO_2$ is first activated to CO *via* RWGS, and then LAOs are obtained through C–C coupling.[20,21] Fe-based catalysts are widely used for $CO_2$ hydrogenation to LAOs due to their combination of Fe-oxides for the RWGS reaction and Fe-carbides for the C–C coupling reaction, as well as low $CH_4$ selectivity.[22,23] Meanwhile, the modified Fe-based catalyst exhibited excellent catalytic activity and olefin selectivity in $CO_2$ hydrogenation reactions.[24,25] This demonstrated the excellent potential of modified Fe-based catalysts in $CO_2$ hydrogenation to LAOs. However, the generated $H_2O$ and $CO_2$ can oxidize the Fe carbides, thereby weakening the C–C bond coupling ability and resulting in insufficient LAOs selectivity. Therefore, the rational construction of Fe-based catalysts for the $CO_2$ hydrogenation to LAOs is essential to improve LAOs selectivity.

Currently, research on Fe-based catalysts for $CO_2$ hydrogenation to LAOs mainly focuses on promoter modification, catalyst structure optimization, and active-site environment modulation.[26–31] The Zn promoter reduced the particle size of Fe-based catalysts and increased the adsorption of $H_2$, thus

---

[a] School of Materials and New Energy, Ningxia University, Yinchuan 750021, Ningxia, China. E-mail: kangzhou_wang@nxu.edu.cn

[b] State Key Laboratory of High-efficiency Utilization of Coal and Green Chemical Engineering, College of Chemistry & Chemical Engineering, Ningxia University, Yinchuan 750021, Ningxia, China. E-mail: zhangjl@nxu.edu.cn

[c] Department of Applied Chemistry, School of Engineering, University of Toyama, Gofuku 3190, Toyama 930-8555, Japan. E-mail: tsubaki@eng.u-toyama.ac.jp

[d] Qingdao Institute of Bioenergy and Bioprocess Technology, Chinese Academy of Sciences, Qingdao 266101, China

[e] College of Chemical Engineering, Qingdao University of Science and Technology, 53 Zhengzhou Road, Qingdao 266042, China

[f] State Key Laboratory of Chemical Resource Engineering, Beijing Key Laboratory of Energy Environmental Catalysis, Beijing University of Chemical Technology, Beijing, 100029, China. E-mail: wangzj@mail.buct.edu.cn

improving $CO_2$ hydrogenation activity.[32] The Na promoter efficiently enhanced CO* and H* activation, facilitated C–C coupling, and suppressed the secondary hydrogenation of olefins, thereby improving both catalytic activity and LAOs selectivity.[33] Meanwhile, the Na promoter could be enriched on the catalyst surface, which can improve olefin selectivity by inhibiting the secondary hydrogenation of primary olefins.[34] Sr and Na co-modified Fe-based catalysts exhibited stable catalytic performance in $CO_2$ hydrogenation to LAOs. $SrCO_3$ promoted the formation and stabilization of the $FeC_x$ phase. Meanwhile, the Sr promoter strengthened electronic interactions between Na and Fe, thereby improving C–O bond dissociation and C–C coupling.[35] A Cu–Fe catalyst consisting of Cu, Fe-oxides and Fe carbides achieved a $C_{4+}^{=}$ selectivity of 66.9% under atmospheric pressure. The synergistic interaction between $Fe_5C_2$ and the Cu–$Fe_5C_2$ interface promoted the generation of long-chain olefins.[36]

Although significant progress has been made in $CO_2$ hydrogenation to LAOs, effective control of C–O bond activation and C–C bond coupling through interface structures remains challenging. Developing highly efficient catalysts to enhance C–C coupling is crucial for improving LAOs selectivity. By modulating promoter content, the active-phase composition ($Fe_3O_4$ and $Fe_5C_2$) can be effectively regulated to optimize RWGS/FTS reaction matching. Fe–Mn–K catalysts exhibited excellent catalytic performance with a $CO_2$ conversion of 32.9% and LAOs selectivity of 45.7%.[37] Significant progress has been made in understanding the stabilizing and promoting effects of Mn on iron carbides in $CO_2$ hydrogenation reactions. The Mn promoter significantly reduced the rates of reduction and carbonization reactions, inducing pronounced reaction-induced evolution of the $Fe_5C_2$ phase. A surface layer of MnO converting $Fe_5C_2$ effectively inhibited $CH_4$ formation, while promoting the production of light olefins and $C_{5+}$ hydrocarbons.[38] Guo *et al.*[30] employed multiple *in situ* techniques to reveal the structural evolution of Fe-based catalysts during $CO_2$ hydrogenation to hydrocarbons. In the initial reduction phase, Fe species undergo carbonization to form $Fe_3C$, which subsequently transforms into $Fe_5C_2$. The generated $H_2O$ during $CO_2$ hydrogenation to LAOs could oxidize $Fe_5C_2$ to the $Fe_3O_4$ phase. The $Fe_5C_2$–$ZrO_2$ interfacial structure enhanced the adsorption of key CO intermediates, forming a CO-enriched microenvironment on the $Fe_5C_2$ active phase surface. This significantly increases the partial pressure of CO on the $Fe_5C_2$ phase, thereby reducing the adsorption energy of $H_2O$ on the $Fe_5C_2$ surface.[39,40] Consequently, it effectively improved catalyst stability and C–C coupling capability. The introduction of Mn promoted the dispersion of Fe species and enhanced the formation of Fe oxides, while the addition of the K promoter favored the generation of Fe carbides, thus improving carbon-chain growth capability. The incorporation of Mn and K effectively modulates the balance between the RWGS and FTS reactions by promoting the formation and conversion of CO intermediates.[37,41] In FeZr catalysts, oxygen vacancies in $ZrO_2$ promote $CO_2$ adsorption and activation.[42] Although significant progress has been achieved with K/FeMn catalysts in $CO_2$ hydrogenation to LAOs, research has mainly focused on regulating the RWGS and FTS active sites through the Mn promoter to achieve high olefin selectivity. In contrast, K–FeZr catalysts primarily modulate $CO_2$ adsorption and $H_2$ dissociation through oxygen vacancies, exhibiting excellent selectivity toward light olefins in $CO_2$ hydrogenation. Therefore, the $Fe_5C_2$–$ZrO_2$ interfacial structure can create a CO-enriched microenvironment at the $Fe_5C_2$ active sites by utilizing the strong CO adsorption capacity of oxygen vacancies on the $ZrO_2$ surface. This effectively increases the partial pressure of CO on the $Fe_5C_2$ surface and reduces the adsorption energy of $H_2O$, thereby suppressing the oxidation of the $Fe_5C_2$ active phase by $H_2O$ and significantly enhancing the C–C coupling capability.[43] Meanwhile, the interfacial structure not only facilitates the transport of key intermediate species, but also lowers the activation energy barrier for C–C coupling.[36] Therefore, constructing $Fe_5C_2$–$ZrO_2$ interfacial catalysts should effectively promote LAOs synthesis in $CO_2$ hydrogenation.

In this work, we report a Na/FeMn/$ZrO_2$ catalyst that demonstrated high catalytic performance for $CO_2$ hydrogenation to LAOs. Under reaction conditions of 320 °C, 1.5 MPa, and 7500 mL $g_{cat}^{-1}$ $h^{-1}$, it achieved a LAOs selectivity in $C_{4+}$ hydrocarbons of 68.0% and an O/P ratio of 5.1. The structure–performance relationships were revealed by various characterization techniques. The strong CO adsorption capacity at the $Fe_5C_2$–$ZrO_2$ interface enriched CO intermediates on $Fe_5C_2$ active sites, promoting C–C coupling reactions. Meanwhile, strong interfacial interactions enhanced synergy among various active sites, resulting in superior selectivity for high-value olefins.

## Results and discussion

### Active phase characterization

The active phase composition of the catalysts was analyzed by XRD. The calcined samples of Fe, Na/Fe, and Na/FeMn exhibited characteristic diffraction peaks of the $Fe_2O_3$ phase (JCPDS, 33-0664) (Fig. S1). However, the diffraction peak intensities of the $Fe_2O_3$ phase in the Na/FeMn/$SiO_2$ and Na/FeMn/$ZrO_2$ catalysts were much weaker (Fig. S1). XRD patterns of the reduced catalysts are shown in Fig. 1. The characteristic diffraction peaks of the Fe phase (JCPDS, 06-0696) appeared in the reduced Fe and Na/Fe catalysts, while a mixed phase of Fe, $FeMnO_x$, and $Mn_2O$ (JCPDS, 07-0230) appeared in the reduced Na/FeMn catalyst. However, no significant Fe phases were detected in

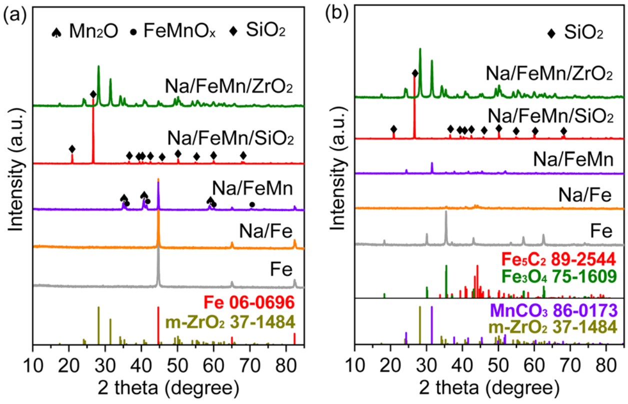

Fig. 1 XRD patterns of the reduced (a) and spent (b) catalysts.

the reduced Na/FeMn/$SiO_2$ and Na/FeMn/$ZrO_2$ catalysts, indicating that the reduced Fe species were uniformly dispersed on $SiO_2$ and $ZrO_2$. Only characteristic diffraction peaks of the $Fe_3O_4$ phase (JCPDS, 75-1609) were detected in the spent Fe catalysts. Compared with the pure Fe catalyst, the Na/Fe catalyst exhibited a weak $Fe_5C_2$ phase (JCPDS, 89-2544), indicating that the Na promoter was beneficial to the formation of the $Fe_5C_2$ phase.[44] The $MnCO_3$ phase (JCPDS, 86-0173) appeared in the spent Na/FeMn catalyst, which stabilized the active phase and improved the catalytic activity owing to the thermal stability and electronic interactions of alkaline earth metal carbonates.[45] No significant Fe carbide phase was detected in the spent Na/FeMn/$SiO_2$ catalysts, because the interaction between Fe species and $SiO_2$ hydroxyl groups from Fe–O–Si bonds was unfavorable for the formation of iron carbides. However, both $Fe_3O_4$ and $Fe_5C_2$ phases (JCPDS, 89-2544) appeared in the spent Na/FeMn/$ZrO_2$ catalyst, indicating that Fe species can be further carbonized to form $Fe_5C_2$. The strong interaction between Fe and $ZrO_2$ could promote iron carbide formation.[40]

*In situ* XRD analysis was performed to reveal the phase evolution during $H_2$ reduction and $CO_2$ hydrogenation reaction processes over the Na/FeMn/$ZrO_2$ catalyst. The characteristic diffraction peaks of $Fe_2O_3$ and $ZrO_2$ were mainly detected on the Na/FeMn/$ZrO_2$ catalyst (Fig. S2). The characteristic diffraction peaks of $Fe_2O_3$ were weak, indicating that the Fe species were uniformly distributed on $ZrO_2$. The interaction between the complex (formed by the ethylene diamine tetraacetic acid and Fe species) and hydroxyl groups at oxygen vacancies of $ZrO_2$ was reported to form small sized $Fe_2O_3$.[46] Increasing the reduction temperature to 350 °C caused disappearance of $Fe_2O_3$ diffraction peaks with no detectable $Fe_3O_4$ diffraction peaks (Fig. 2a). That is, $Fe_2O_3$ could be completely reduced at 400 °C and the reduced Fe species were uniformly dispersed on the $ZrO_2$ surface. After reduction, the system was cooled to 320 °C and then the feedstock ($H_2/CO_2 = 3$) was introduced. As the reaction progressed, the characteristic peaks of $Fe_3O_4$, $Fe_5C_2$, and $MnCO_3$ appeared. The reappearance of $Fe_3O_4$ was attributed to the oxidation of FeO or Fe during the reaction (Fig. 2b). The resultant $Fe_3O_4$ and $Fe_5C_2$ were the active sites for the RWGS and FTS reactions, respectively. Importantly, $ZrO_2$ remained unchanged in its monoclinic phase, indicating its stable presence during the $CO_2$ hydrogenation reaction (Fig. S3).

## Morphology and textural characteristics

SEM images clearly exhibited the microscopic morphology of the catalysts. The fresh Na/FeMn/$ZrO_2$ catalysts exhibited a stack of spherical nanoparticles around 50 nm (Fig. S4). Compared with the fresh Na/FeMn/$ZrO_2$ catalyst, the spent catalyst displayed larger particles and elongated crystals, due to the formation of some $MnCO_3$ and $FeMnO_x$ species during the reaction. The microstructure of fresh and spent Na/FeMn/$ZrO_2$ catalysts was further characterized using the HR-TEM technique, and the results are shown in Fig. 3 and S5. The fresh Na/FeMn/$ZrO_2$ catalysts possessed an irregular crystal structure with rough edges, and the particle size of the Na/FeMn/$ZrO_2$ catalysts increased after the reaction (Fig. 3a and c). The intimacy of catalyst components had a great influence on the catalyst performance. The HAADF-STEM images and the corresponding EDS elemental maps of the fresh and spent Na/FeMn/$ZrO_2$ catalysts were analyzed in detail. The elements Fe, Mn, and Na in the Na/FeMn/$ZrO_2$ catalysts were almost uniformly distributed on the $ZrO_2$ support (Fig. 3e and S5).

Meanwhile, Na, Fe, Mn, and Zr species exhibited relatively close contact (Fig. S6). The closely packed $MnCO_3$ effectively stabilized the $Fe_5C_2$ active phase, inhibiting the oxidation that generated $H_2O$ molecules and thereby promoting C–C coupling reactions.[47] To further characterize the $Fe_5C_2$–$ZrO_2$ interface structure, EDS mapping of Fe and Zr elements was performed (Fig. S7). The mapping of Fe and Zr in the Na/FeMn/$ZrO_2$ catalyst clearly revealed an interfacial structure.

To further elucidate the elemental composition of the catalyst, ICP analysis was performed, and the results are summarized in Table S1. The elemental compositions of the Na/FeMn, Na/FeMn/$SiO_2$, and Na/FeMn/$ZrO_2$ catalysts were found to be consistent with theoretical values. The surface area and pore size distribution of the synthesized catalysts were analyzed

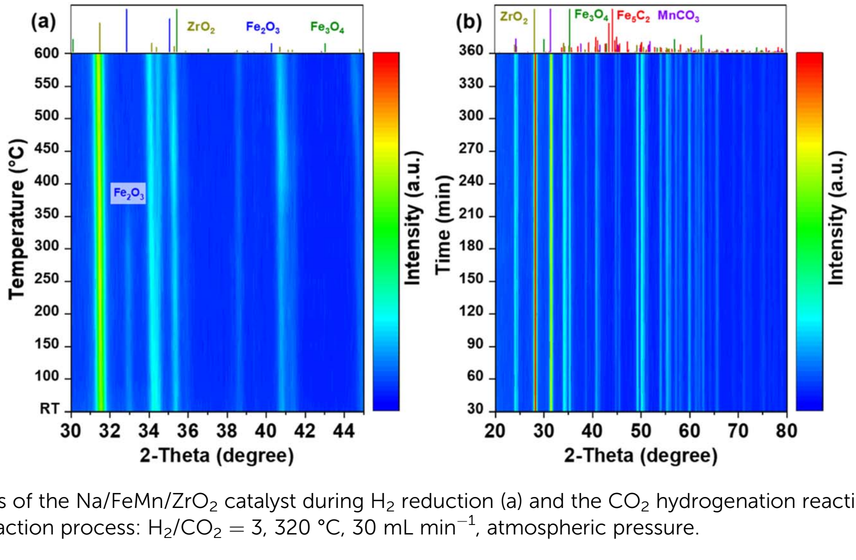

Fig. 2 *In situ* XRD patterns of the Na/FeMn/$ZrO_2$ catalyst during $H_2$ reduction (a) and the $CO_2$ hydrogenation reaction (b). Reduction process: pure $H_2$, 30 mL min$^{-1}$. Reaction process: $H_2/CO_2 = 3$, 320 °C, 30 mL min$^{-1}$, atmospheric pressure.

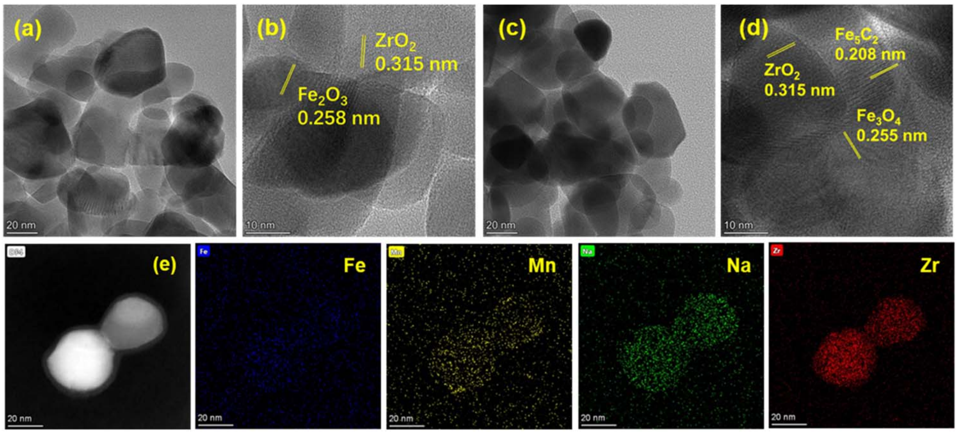

Fig. 3 TEM images of the fresh (a and b) and spent (c and d) Na/FeMn/$ZrO_2$ catalysts. STEM image of the spent Na/FeMn/$ZrO_2$ catalyst (e) and the corresponding EDS elemental mapping images.

using $N_2$ adsorption–desorption measurements, and the results are summarized in Table S2. The addition of the Na promoter to the Fe catalyst increased its specific surface area (from 23.7 $m^2\ g^{-1}$ to 25.0 $m^2\ g^{-1}$) and enlarged the average pore size from 11.5 nm to 13.8 nm. Compared with Na/Fe, Na/FeMn exhibited smaller specific surface area, pore size, and pore volume due to nanoparticle aggregation caused by the promoter. Na/FeMn/$SiO_2$ catalysts had the smallest specific surface area and pore size. Relative to Na/FeMn, Na/FeMn/$ZrO_2$ showed significantly higher specific surface area and pore volume alongside reduced pore size. These changes indicate that $ZrO_2$ improved the dispersion of active sites by increasing the specific surface area, which was beneficial for the reaction and diffusion of feedstocks/intermediates.

## Chemical state, reduction and chemisorption behavior

To determine the chemical state of the catalyst, we carried out XPS analysis of the spent catalysts with the results shown in Fig. 4. The binding energies of the Fe 2p spectra of all spent catalysts exhibited two characteristic peaks at 710.8 eV and 723.9 eV, which were assigned to Fe $2p_{3/2}$ and Fe $2p_{1/2}$ of iron oxide species, respectively (Fig. 4a).[48] The Na/Fe, Na/FeMn, Na/FeMn/$SiO_2$, and Na/FeMn/$ZrO_2$ catalysts displayed characteristic peaks at 706.8 eV, which were attributed to Fe carbide species.[48] No characteristic peaks of Fe carbide were detected in the fresh catalyst and the reduced catalyst. Meanwhile, no such signal was detected in the Fe catalyst, indicating that Na and Mn promoters play a crucial role in the formation of Fe carbide species. Mn 2p XPS spectra exhibited two characteristic peaks at 641.7 eV and 653.5 eV, which corresponded to Mn $2p_{3/2}$ and Mn $2p_{1/2}$ of manganese oxide species, respectively (Fig. S8). However, the spent catalysts displayed two shoulder peaks, which were attributed to the characteristic features of $Mn^{2+}$ in $MnCO_3$ species (Fig. S8). Notably, the C 1s binding energy of Na/FeMn, Na/FeMn/$SiO_2$, and Na/FeMn/$ZrO_2$ catalysts shifted to 289.2 eV, which was higher than that of Fe and NaFe catalysts (at 288.7 eV) (Fig. 4b). The apparent change in binding energy further revealed strong electron transfer and interfacial interaction between Fe species and Mn species.[30] The O 1s spectra displayed two characteristic peaks corresponding to oxygen vacancy and lattice oxygen, appearing at 532.1 and 529.6 eV, respectively (Fig. 4c and S11).[49] Fresh Na/FeMn samples show higher oxygen vacancies and lattice oxygen, while fresh Na/FeMn/$SiO_2$ samples predominantly contain lattice oxygen. After reduction, the oxygen vacancies in the Na/FeMn catalyst decreased significantly, while those in Na/FeMn/$SiO_2$ and Na/FeMn/$ZrO_2$ samples increased. The oxygen vacancy was beneficial to the $CO_2$ activation.[50] Although the spent Na/FeMn/$SiO_2$ sample possessed abundant oxygen vacancies, its catalytic activity and olefin selectivity were relatively low. This was primarily attributed to Fe species interacting with silicon hydroxyl groups to form $Fe_2SiO_4$, which was difficult to further reduce into $Fe_5C_2$, resulting in insufficient C–C coupling active sites in the Na/FeMn/$SiO_2$ catalyst.[51,52] The Zr 3d binding energy of Na/FeMn/$ZrO_2$ exhibited two peaks at 183.8 eV and 181.4 eV, which were attributed to $ZrO_2$ species (Fig. S12). The binding energy of the Si 2p spectra of Na/FeMn/$SiO_2$ appeared at 101.8 eV, which was associated with $SiO_2$ species (Fig. S13). These results indicated that Mn and $ZrO_2$ promoted the dissociation of lattice oxygen to generate oxygen vacancies during the reduction process, thereby improving CO intermediate adsorption and C–C coupling. The surface elemental compositions of the spent catalyst are listed in Table S3. Compared with Fe, the Na/Fe catalyst exhibited lower surface Fe content and higher C content, indicating that the Na promoter enhanced the carbonization capability of Fe species. With the introduction of the Mn promoter, the surface Fe content decreased, which was attributed to the Mn species migrating to the surface of Fe species.[38] Compared with the Na/FeMn/$SiO_2$ catalyst, the Na/FeMn/$ZrO_2$ catalyst exhibited higher carbon content, indicating greater susceptibility to carbonization and formation of $Fe_5C_2$ active sites.

$H_2$-TPR experiments were performed to evaluate the interactions between the species. In Fig. 4d, $H_2$ consumption peaks at 365 °C and 527 °C for the Fe catalyst represented the gradual reduction of $Fe_2O_3$ to Fe. Specifically, the $H_2$ consumption peak at 365 °C was attributed to the reduction of $Fe_2O_3$ to $Fe_3O_4$, while the broad peak near 527 °C was attributed to the

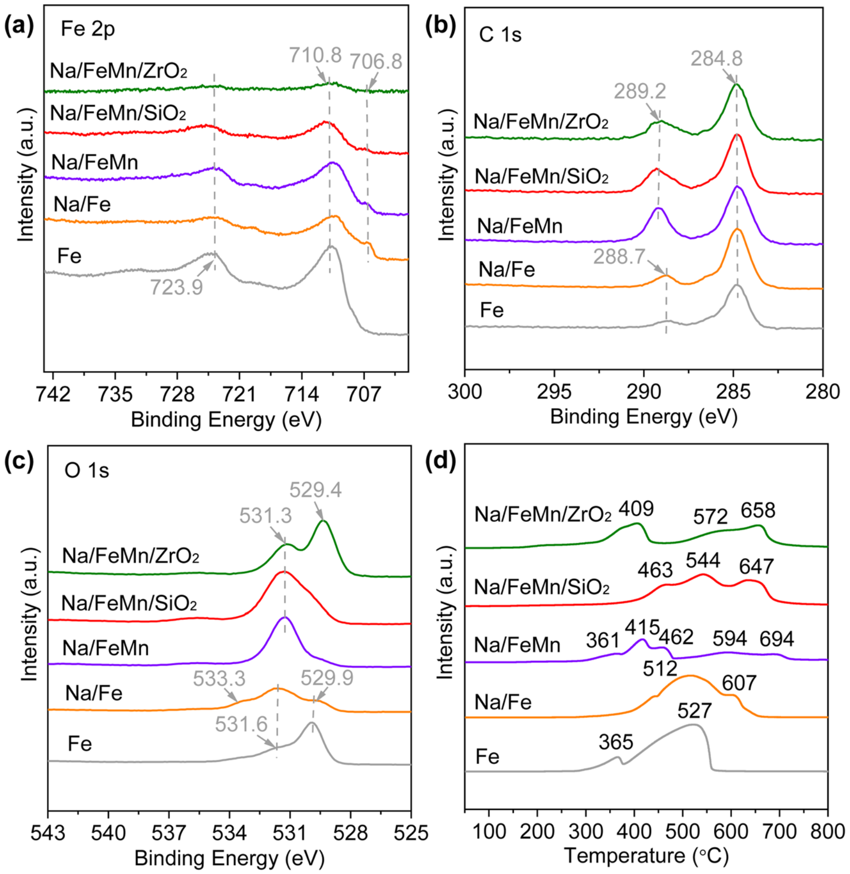

Fig. 4 Fe 2p (a), C 1s (b), and O 1s (c) XPS spectra of the spent catalysts. (d) $H_2$-TPR profiles of the synthesized catalysts.

reduction of $Fe_3O_4$ to FeO and the further reduction of FeO to Fe. Compared with the Fe catalyst, Na/Fe exhibited a $H_2$ consumption peak with higher temperature, indicating that the Na promoter inhibited the reduction of $Fe_2O_3$. $MnO_2$ samples exhibited three reduction peaks at 308 °C, 422 °C, and 510 °C (Fig. S14). The reduction peak at 361 °C for Na/FeMn was weakened, while the high-temperature peaks increased, indicating that the transition metal enhanced the Fe–O bond energy.[53] For the Na/FeMn catalyst, $H_2$ consumption peaks near 361 °C and 462 °C were attributed to the reduction of Mn species. Relative to the Na/Fe catalyst, the Na/FeMn catalyst exhibited significantly lower $H_2$ consumption, with all Fe species reduction peaks shifting to higher temperatures. This indicates that Mn species strengthened the Fe–O bond energy.[54] In comparison, the reduction peaks of the Na/FeMn/$SiO_2$ catalysts all shifted to high temperature, which was attributed to the formation of the Fe–O–Si bond.[55] Compared with Na/FeMn catalysts, the reduction peak of the Na/FeMn/$ZrO_2$ catalyst shifted to a lower temperature, which was beneficial to the reduction of Fe species.[53] This shift was attributed to $ZrO_2$ enhancing the migration and reactivity of hydrogen species.[56] These results further indicated strong interactions among Fe, Mn, and Zr species, which had a positive effect on the stability of iron carbide species. The $H_2$ consumption of as-prepared catalysts is summarized in Table S4. Compared with the Fe catalyst, the Na/Fe catalyst exhibited lower low-temperature $H_2$ consumption and higher high-temperature $H_2$ consumption. The introduction of the Mn promoter enhanced the formation of $FeMnO_x$ spinel, which hindered the reduction of both Fe and Mn species, leading to decreased $H_2$ consumption. The $H_2$ consumption of Na/FeMn/$SiO_2$ and Na/FeMn/$ZrO_2$ decreased due to reduced Fe content from the introduced supports. Compared with Na/FeMn/$SiO_2$, the Na/FeMn/$ZrO_2$ catalyst exhibited higher low-temperature $H_2$ consumption, while lower high-temperature consumption, indicating greater susceptibility to $H_2$ reduction.

To elucidate the CO adsorption of the Na/FeMn/$ZrO_2$ catalyst, CO-TPD analysis was performed on reference $ZrO_2$ and Na/FeMn/$ZrO_2$ catalysts (Fig. S15). The $ZrO_2$ sample exhibited a weak CO desorption peak at 291 °C, indicating its relatively low CO adsorption. Compared with the $ZrO_2$ sample, the Na/FeMn/$ZrO_2$ catalyst exhibited a pronounced CO desorption peak at 313 °C, indicating that the Na/FeMn/$ZrO_2$ catalyst with an $Fe_5C_2$–$ZrO_2$ interfacial structure possesses strong CO adsorption. The strong adsorption capacity for CO enabled the formation of a high partial pressure of CO on the surface of the Na/FeMn/$ZrO_2$ catalyst, thereby inhibiting the adsorption of $H_2O$ molecules on the $Fe_5C_2$ active sites and effectively promoting the C–C coupling reaction.[43] CO-DRIFTS was employed to further investigate the adsorption configuration and strength of CO on the surface of the Na/FeMn/$ZrO_2$ catalyst (Fig. S16). The adsorption and desorption spectra of the Na/FeMn/$ZrO_2$ catalyst exhibited peaks at 2170 $cm^{-1}$ and

2118 $cm^{-1}$, respectively, which was attributed to the adsorption of gaseous CO. Peaks observed at 2068 $cm^{-1}$, 2054 $cm^{-1}$, and 2031 $cm^{-1}$ correspond to linear CO adsorption. These linear CO adsorption peaks markedly intensify with extended adsorption time. The adsorbed CO could enhance the partial pressure of CO at the $Fe_5C_2$ active sites, thereby promoting C–C coupling reactions.[43,57]

The effective adsorption of $CO_2$ on the active sites of the catalysts could promote the activation of C–O bonds and the generation of CO intermediates. $CO_2$-TPD analysis was employed to elucidate $CO_2$ adsorption behavior of the catalysts (Fig. S17). The Na/Fe catalyst displayed two desorption peaks, where the low- and high-temperature peaks were attributed to the interaction of $CO_2$ molecules with weak and strong base sites, respectively. Compared with the Na/Fe catalyst, Na/FeMn catalysts exhibited stronger $CO_2$ desorption peaks at 200 °C, suggesting that Na and Mn promoters enhanced $CO_2$ adsorption. The desorption peak of $CO_2$ for the Na/FeMn/$SiO_2$ catalyst was significantly weakened, indicating that the Na/FeMn/$SiO_2$ catalyst had a weaker adsorption capacity for $CO_2$.[58] The Na/FeMn/$ZrO_2$ catalyst exhibited a strong $CO_2$ desorption peak near 100 °C, indicating that the introduction of $ZrO_2$ increased $CO_2$ adsorption capacity despite weak binding strength. These results indicated that the introduction of Mn species and $ZrO_2$ modulated the amount and strength of $CO_2$ adsorption.[59] The suitable $CO_2$ adsorption on catalyst active sites promoted the generation of Fe-carbide active phases, which improved the yield of high-value olefins.

### Mössbauer spectroscopy analysis

$^{57}$Fe Mössbauer spectroscopy of the spent Na/FeMn/$ZrO_2$ catalysts further identified the Fe species in the catalysts, and the results are shown in Fig. 5. The detailed composition and comparison of the different phases are listed in Table S5. Small amounts of $Fe_3O_4$ species were contained in the spent Na/FeMn/$ZrO_2$ catalysts, which were mainly detected as $Fe_5C_2$(II), $Fe_5C_2$(I), and $Fe_5C_2$(III), accounting for 31.7%, 26.2%, and 29.9%, respectively.[60–62] Therefore, the synergistic effect of $Fe_5C_2$ and $Fe_3O_4$ active sites promoted the highly selective synthesis of high value olefins from $CO_2$ hydrogenation.

To further investigate the adsorption, activation, and dissociation strength of CO intermediates, $H_2$-TPSR measurements were performed on the Na/FeMn and Na/FeMn/$ZrO_2$ catalysts. In Fig. 5b, the Na/FeMn catalyst exhibited two CO desorption peaks, and the desorption peaks were primarily concentrated in the temperature range of 450 °C to 750 °C. Relative to Na/FeMn, Na/FeMn/$ZrO_2$ exhibited attenuated CO desorption intensity with peaks shifting to higher temperatures, providing evidence of strengthened CO adsorption. Consequently, substantial CO accumulated at the $Fe_5C_2$–$ZrO_2$ interface, where it rapidly migrated to $Fe_5C_2$ sites, facilitating C–C coupling reactions. Meanwhile, two $H_2$ consumption peaks appeared on the surface of the Na/FeMn catalyst. The $H_2$ consumption of the Na/FeMn/$ZrO_2$ catalyst significantly increased, indicating that the enriched CO underwent dissociation. These results indicated that the Na/FeMn/$ZrO_2$ catalyst with an $Fe_5C_2$–$ZrO_2$ interfacial structure could enrich CO at the interface. The enriched CO underwent dissociation and C–C coupling at $Fe_5C_2$ active sites, promoting $CO_2$ hydrogenation toward high-value olefins.

### Catalytic performance

The catalytic performance of the prepared catalysts for $CO_2$ hydrogenation to LAOs is shown in Fig. 6. Detailed results on product distribution, O/P ratio, and LAOs yield are summarized in Table S6. The Fe catalyst exhibited a $CO_2$ conversion of 29.3%, a LAOs/$C_{4+}$ ratio of 4.1%, and a LAOs yield of 0.2%. Compared with the Fe catalyst, Na/Fe displayed significantly higher $CO_2$ conversion and $C_{5+}$ selectivity, alongside markedly lower $CH_4$ selectivity and LAOs selectivity (Fig. 6a). Na content impacts $CO_2$ hydrogenation by reducing the hydrogen adsorption and activation capacity, thereby reducing the coverage of hydrogen species.[63] The primary reaction of $CO_2$ hydrogenation is suppressed. Compared with the unpromoted Fe catalyst, Na/Fe catalysts exhibited lower selectivity toward $CH_4$ and $C_2$–$C_4$ hydrocarbons. The inhibitory effect of Na on $CH_4$ and light alkane formation could be attributed to its regulation of the electronic properties of iron carbides, which enhanced the generation of surface carbon-containing species and hydrogen-containing species.[64] Furthermore, the Na promoter was beneficial to the production of $C_{5+}$ hydrocarbons by modulating the

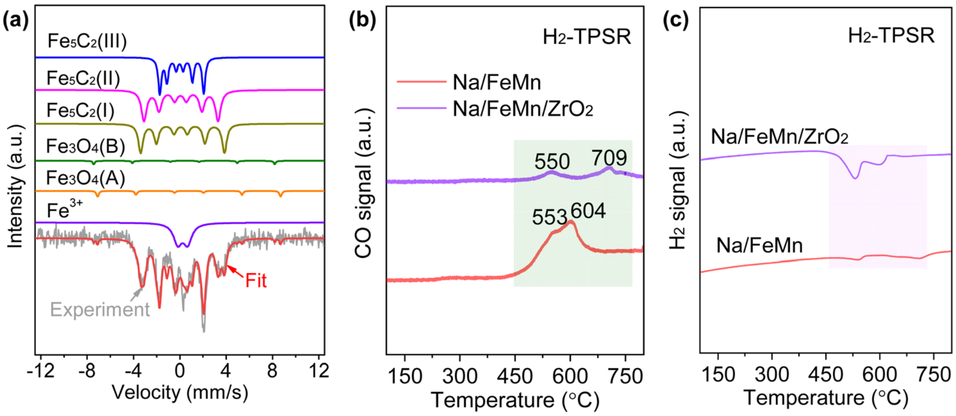

Fig. 5 $^{57}$Fe Mössbauer results of the spent Na/FeMn/$ZrO_2$ catalyst (a); CO signal (b) and $H_2$ signal (c) under CO pre-adsorption and $H_2$-TPSR measurements.

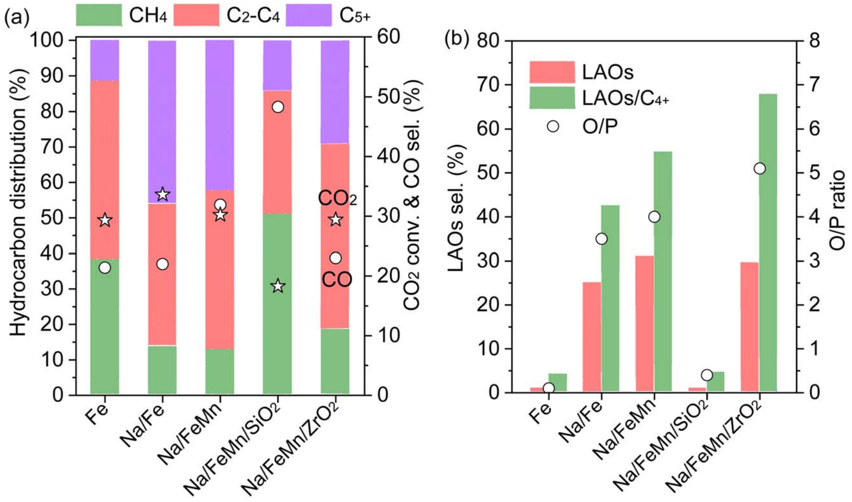

Fig. 6 Catalytic performance toward $CO_2$ hydrogenation. (a) The hydrocarbon distribution, $CO_2$ conversion, and CO selectivity. (b) LAOs selectivity, LAOs/$C_{4+}$ ratio, and O/P ratio of catalysts. Reaction conditions: $H_2/CO_2 = 3$, 1.5 MPa, 320 °C, 7500 mL $g_{cat}^{-1}$ $h^{-1}$, TOS = 10 h. The LAOs/$C_{4+}$ ratio represents the LAO fraction within the $C_{4+}$ hydrocarbons.

surface carbon-to-hydrogen ratio, primarily following a catalytic surface polymerization mechanism.[65] The promotion of CO disproportionation (Boudouard reaction) also increased carbonization in Na-promoted catalysts, facilitating the formation of $Fe_5C_2$ and accelerating C–C coupling reactions.[66] The Na/FeMn catalyst exhibited higher catalytic activity and LAOs selectivity with a $CO_2$ conversion of 30.2%, a LAOs/$C_{4+}$ selectivity of 54.8%, a light olefin selectivity of 35.9%, and a LAOs yield of 6.3%. The introduction of the Na promoter decreased $CH_4$ selectivity from 38.2% to 22.0%, which was attributed to the electron transfer from Na to the $Fe_5C_2$ phase. The resulting increase in electron density at Fe sites facilitated the CO dissociation and destabilized adsorbed H atoms on the Fe surface, thereby promoting the hydrogenation of carbon species.[67] The introduction of Mn further enhanced the electron-donating ability of Na and promoted the formation of $MnCO_3$, leading to Na enrichment on the $Fe_5C_2$ surface and providing abundant basic sites. The steric hindrance effect induced by high-density sodium enrichment on the $Fe_5C_2$ surface impairs chain growth capability.[47] Studies indicated that Na and Mn synergistic effects could enhance RWGS and FTS. Nevertheless, as the Mn/Fe molar ratio increased from 1 : 3 to 1 : 1, CO selectivity reverses, suggesting that higher Mn content weakens FTS activity. Compared with the Na/Fe catalyst, the Na/FeMn catalyst exhibited lower $CO_2$ conversion and higher CO selectivity. This decline in activity was likely due to coverage of active sites by the Mn promoter. When Mn was added to the Na/Fe catalyst, Mn species dispersed uniformly on the $Fe_5C_2$ surface. The steric hindrance caused by these Mn species reduced the ability of intermediates to undergo C–C coupling on the $Fe_5C_2$ phase, thereby inhibiting the formation of $C_{5+}$ hydrocarbons.[68] The suppressed C–C coupling allowed CO generated *via* RWGS to accumulate, increasing CO selectivity. These results are consistent with those reported in the literature.[68] Compared with the Na/FeMn catalyst, Na/FeMn/$SiO_2$ showed significantly lower $CO_2$ conversion and LAOs selectivity but higher CO selectivity. This resulted from different reduction/activation of Fe species, which limited chain growth active sites and prevented the generated CO from being activated to undergo C–C coupling for the formation of LAOs.[69] The Na/FeMn/$ZrO_2$ catalyst possessed higher $CO_2$ conversion and LAOs selectivity, but lower CO and $CH_4$ selectivity than Na/FeMn/$SiO_2$ (Fig. S18). Among these catalysts, the Na/FeMn/$ZrO_2$ catalyst possessed a higher LAOs yield of 6.7%. Importantly, the LAOs/$C_{4+}$ selectivity and O/P ratio of the Na/FeMn/$ZrO_2$ catalyst reached 68.0% and 5.1, respectively (Fig. 6b). For the $C_{2+}$ product distribution, the Fe catalyst had higher selectivity for light alkanes, while Na/Fe exhibited higher light olefin selectivity and $C_{5+}$ alkane selectivity. With Mn promotion, the Na/FeMn catalyst showed significantly higher light olefin and $C_{5+}$ olefin yields than Na/Fe. This indicated that Na and Mn promoters suppressed secondary hydrogenation of primary olefins, thereby boosting selectivity toward high-value olefins. Among these catalysts, the Na/FeMn/$ZrO_2$ catalyst possessed the highest high-value olefin selectivity (61.3%) and O/P ratio (5.1). The $Fe_5C_2$–$ZrO_2$ interfacial structure effectively enhanced the synergism among various active sites and CO intermediate adsorption. Moreover, the CO generated by the RWGS reaction on FeMn sites could be effectively adsorbed at this interface. The significantly increased CO partial pressure on $Fe_5C_2$ enhanced C–C coupling capability while suppressing olefin secondary hydrogenation, thereby promoting high-value olefin formation and specifically improving LAOs selectivity.

## Reaction mechanism for $CO_2$ hydrogenation to LAOs

Compared with other investigated catalysts, Na/FeMn/$ZrO_2$ exhibited the best high-value olefin selectivity in $CO_2$ hydrogenation. To reveal the key intermediate species during the reaction, *in situ* DRIFTS analysis was performed over Na/FeMn/$ZrO_2$. The peaks in the wavenumber range of 2400 $cm^{-1}$ to 2300 $cm^{-1}$ were attributed to the adsorption of gaseous $CO_2$ (Fig. S19), indicating that the catalyst possessed a strong adsorption capacity for $CO_2$ molecules.[25] As shown in Fig. 7, the vibrational peaks in the range of 1710–1200 $cm^{-1}$ were assigned to the adsorbed carbonate and formate species ($CO_3^*$, $HCO_3^*$ and HCOO*). These intermediates were formed through the interaction of oxygen vacancies on the catalyst surface with $CO_2$.[70] The vibration peak at 1672 $cm^{-1}$ was attributed to the symmetric and asymmetric stretching vibrations of the bidentate carbonate species. As the reaction proceeded, vibration peaks corresponding to carbonate ($CO_3^*$) and bicarbonate ($HCO_3^*$) species appeared at 1370 $cm^{-1}$ and 1308 $cm^{-1}$.[71] At a reaction temperature of 200 °C (Fig. 7a), the vibration peaks at 1370 $cm^{-1}$ and 1297 $cm^{-1}$ did not change significantly as the reaction proceeded. This result indicated that the generated $CO_3^*$ species did not fully participate in the subsequent reaction. At a higher reaction temperature of 320 °C (Fig. 7b), the vibrational peaks of $CO_3^*$ species gradually increased as the reaction proceeded, indicating that the initially generated $CO_3^*$ species were rapidly involved in the subsequent reaction. CO intermediates enriched at the $Fe_5C_2$ active site were beneficial to the C–C coupling.

To further demonstrate CO enrichment on $Fe_5C_2$ active sites enabled by the $Fe_5C_2$–$ZrO_2$ interface, we compared CO adsorption energies on $Fe_5C_2$ and $Fe_5C_2$–$ZrO_2$ using density functional theory (DFT) calculations. To simulate the $Fe_5C_2$–$ZrO_2$ interface, we constructed $Fe_5C_2(11{-}2)$ on the $ZrO_2(-111)$ surface (Fig. S20). As depicted in Fig. 7c, the CO adsorption energy on $Fe_5C_2$ and the $Fe_5C_2$–$ZrO_2$ interface was 1.97 eV and 2.12 eV, respectively. The higher CO adsorption energy on the $Fe_5C_2$–$ZrO_2$ interface suggested stronger CO adsorption capacity. The $Fe_5C_2$–$ZrO_2$ interface promoted CO adsorption, thereby enriching CO at the $Fe_5C_2$ active sites. The enriched CO could accelerate the occurrence of C–C coupling reactions. To gain a deeper understanding of the reaction mechanism, we calculated the energy barrier for C–C coupling. $CO_2$ hydrogenation to high value olefins is a complex process involving multiple possible steps. For simplicity, we employed $CH_2 + CH_2$ to represent the C–C coupling reaction between $CH_2$ intermediates. The energy barrier for $CH_2$ insertion on the $Fe_5C_2$ surface reached up to 0.81 eV. For the $Fe_5C_2$–$ZrO_2$ interface, the energy barrier for $CH_2$ insertion decreased to 0.64 eV. These results indicated that the $Fe_5C_2$–$ZrO_2$ interface not only enabled CO enrichment at $Fe_5C_2$ active sites, but also lowered the C–C coupling energy barrier, thereby promoting C–C coupling reactions toward high-value olefin production. Therefore, the possible reaction pathways for $CO_2$ hydrogenation to high-value olefins on Na/FeMn/$ZrO_2$ catalysts with $Fe_5C_2$–$ZrO_2$ interface structures are proposed in Fig. 7e. Notably, the synergistic action of each active

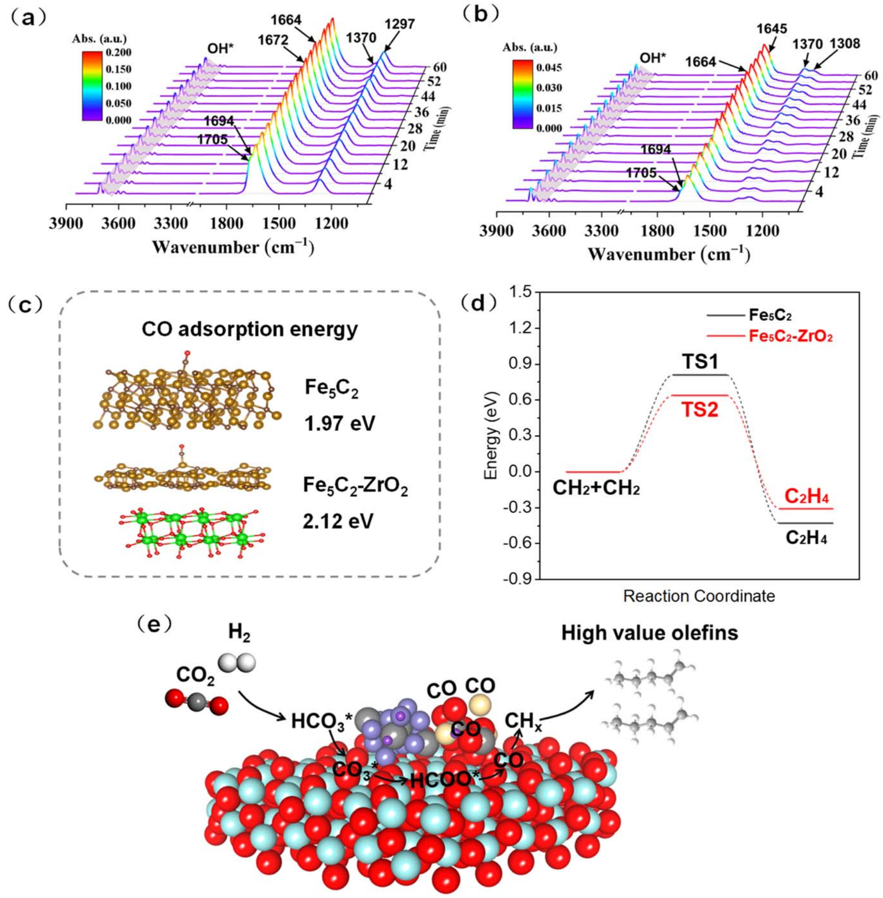

Fig. 7 *In situ* DRIFTS of $CO_2$ hydrogenation to LAOs over the Na/FeMn/$ZrO_2$ catalyst. (a) $H_2/CO_2 = 3$, 200 °C, 30 mL $min^{-1}$ (b) $H_2/CO_2 = 3$, 320 °C, 30 mL $min^{-1}$ (reduced conditions: 400 °C, $H_2$, 30 mL $min^{-1}$). (c) CO adsorption energy at the $Fe_5C_2$ and $Fe_5C_2$–$ZrO_2$ interfaces. (d) Comparison of energy barriers of $CH_2 + CH_2$ over $Fe_5C_2$ and the $Fe_5C_2$–$ZrO_2$ interface. (e) Reaction scheme for high-value olefin synthesis from $CO_2$ hydrogenation over the Na/FeMn/$ZrO_2$ catalyst.

sites promoted the RWGS and FTS reactions of $CO_2$ hydrogenation. $CO_2$ was adsorbed on the active sites as carbonate species, which underwent hydrogenation to bicarbonate and subsequently to formate species, followed by further hydrogenation yielding dissociated CO intermediates. The CO generated *via* RWGS was further hydrogenated into $CH_x^*$ species on iron carbide active sites, and then proceeded to C–C coupling for the formation of high-value olefins. Importantly, $Fe_5C_2$–$ZrO_2$ significantly enhanced CO adsorption capacity, enriching CO intermediates on $Fe_5C_2$ active sites and selectively promoting C–C coupling reactions, thereby producing high-value olefins.

## Conclusions

In this work, a Na/FeMn/$ZrO_2$ catalyst featuring an $Fe_5C_2$–$ZrO_2$ interfacial structure was prepared *via* a covalent anchoring strategy. This catalyst exhibited excellent LAOs selectivity and O/P ratio in the directed hydrogenation of $CO_2$ to LAOs, achieving a LAOs/$C_{4+}$ selectivity of 68% and an O/P ratio of 5.1. During reduction, Mn and $ZrO_2$ promoted oxygen vacancy formation through lattice oxygen dissociation, thereby enhancing $CO_2$ adsorption and C–O bond activation. The strong interaction between Fe species and $MnCO_3$, driven by the electronic effect of alkaline earth metal carbonates, effectively improved the catalytic activity. Concurrently, the $Fe_5C_2$–$ZrO_2$ interfaces demonstrated stronger CO adsorption capacity. Elevated CO partial pressure on the $Fe_5C_2$ surface facilitated the C–C coupling reaction. The synergistic interplay of multiple active sites suppressed the secondary hydrogenation of primary olefins while effectively promoting the generation of LAOs.

## Author contributions

Kangzhou Wang: investigation, formal analysis, writing – original draft. Tong Liu: investigation. Pengqi Hai: software. Shunnosuke Fujii: investigation. Chufeng Liu: formal analysis. Hanyao Song: methodology. Caixia Zhu: investigation. Guangbo Liu: supervision. Jianli Zhang: funding acquisition. Zhou-jun Wang: writing – review & editing. Noritatsu Tsubaki: writing – review & editing.

## Conflicts of interest

There are no conflicts to declare.

## Data availability

The authors confirm that the data supporting the findings of this study are available within the article and its supplementary information (SI). Supplementary information is available. See DOI: https://doi.org/10.1039/d5sc08926c.

## Acknowledgements

This work was financially supported in part by the National Natural Science Foundation of China (22368041 and 22378017), the Key Research and Development Program of Ningxia (Talent-Introduction Program, 2023BSB03061), and the Ningxia Natural Science Foundation (2024AAC03049). P. Hai acknowledges the Hefei Advanced Computing Center.

## Notes and references

1 G. A. Meehl, W. M. Washington, W. D. Collins, J. M. Arblaster, A. Hu, L. E. Buja, W. G. Strand and H. Teng, *Science*, 2005, **307**, 1769–1772.

2 H. He, R. J. Kramer, B. J. Soden and N. Jeevanjee, *Science*, 2023, **382**, 1051–1056.

3 K. Wang, H. Oe, Y. Nakaji, Y. Wang, T. Nakaji-Hirabayashi and N. Tsubaki, *Chem*, 2024, **10**, 419–426.

4 W. Zhou, K. Cheng, J. Kang, C. Zhou, V. Subramanian, Q. Zhang and Y. Wang, *Chem. Soc. Rev.*, 2019, **48**, 3193–3228.

5 C. Y. Sun, W. Li and H. Q. Wang, *Rare Met.*, 2024, **43**, 410–412.

6 K. Wang, Z. Li, X. Gao, Q. Ma, J. Zhang, T. Zhao and N. Tsubaki, *Environ. Res.*, 2024, **242**, 117715.

7 N. Liu, J. Wei, J. Xu, Y. J. Yu, Y. Han, K. Wang, J. I. Orege, Q. Ge and J. Sun, *Appl. Catal., B*, 2023, **328**, 122476.

8 M. Cui, Q. Qian, J. Zhang, Y. Wang, B. B. A. Bediako, H. Liu and B. Han, *Chem*, 2021, **7**, 726–737.

9 T. Liu, K. Wang, Z. Liu, H. Feng, C. Liu, H. Song, D. Liang, T. Yang, K. Liu, X. Gao, J. Zhang and N. Tsubaki, *AIChE J.*, 2025, e70051.

10 X. Wang, Y. Man, R. Zhang, C. Cui, K. Wang and Z. Wang, *Chem. Eng. J.*, 2025, **505**, 159458.

11 D. Wang, Z. Xie, M. D. Porosoff and J. G. Chen, *Chem*, 2021, **7**, 2277–2311.

12 Y. Jiang, K. Wang, Y. Wang, Z. Liu, X. Gao, J. Zhang, Q. Ma, S. Fan, T. Zhao and M. Yao, *J. CO2 Util.*, 2023, **67**, 102321.

13 J. Wei, Q. Ge, R. Yao, Z. Wen, C. Fang, L. Guo, H. Xu and J. Sun, *Nat. Commun.*, 2017, **8**, 15174.

14 S. Kattel, P. J. Ramírez, J. G. Chen, J. A. Rodriguez and P. Liu, *Science*, 2017, **355**, 1296–1299.

15 B. Yao, T. Xiao, O. A. Makgae, X. Jie, S. Gonzalez-Cortes, S. Guan, A. I. Kirkland, J. R. Dilworth, H. A. Al-Megren, S. M. Alshihri, P. J. Dobson, G. P. Owen, J. M. Thomas and P. P. Edwards, *Nat. Commun.*, 2020, **11**, 6395.

16 T. Liu, K. Wang, W. Zhang, W. Song, F. Bo, C. Li, Q. Ma, X. Gao, T. Zhao and J. Zhang, *J. Environ. Chem. Eng.*, 2024, **12**, 113885.

17 J. Wang, Y. Xu, G. Ma, J. Lin, H. Wang, C. Zhang and M. Ding, *ACS Appl. Mater. Interfaces*, 2018, **10**, 43578.

18 S. Wang, T. Wu, J. Lin, Y. Ji, S. Yan, Y. Pei, S. Xie, B. Zong and M. Qiao, *ACS Catal.*, 2020, **10**, 6389–6401.

19 B. Liu, J. Liang, X. Gao, Q. Ma, J. Zhang and T. Zhao, *Fuel*, 2022, **326**, 125054.

20 J. Liang, J. Liu, L. Guo, W. Wang, C. Wang, W. Gao, X. Guo, Y. He, G. Yang, B. Liang and N. Tsubaki, *Nat. Commun.*, 2024, **15**, 512.

21 T. Witoon, V. Lapkeatseree, T. Numpilai, C. K. Cheng and J. Limtrakul, *Chem. Eng. J.*, 2022, **428**, 131389.

22 L. Wang, Y. Han, J. Wei, Q. Ge, S. Lu, Y. Mao and J. Sun, *Appl. Catal., B*, 2023, **328**, 122506.

23 J. Zhu, M. Mu, Y. Liu, M. Zhang, G. Zhang, Z. Cheng, B. Yin, A. C. K. Yip, C. Song and X. Guo, *Chem. Eng. Sci.*, 2023, **282**, 119228.

24 K. Wang, Z. Li, T. Liu, X. Gao, T. Yang, K. Liu, X. Gao, Q. Ma, J. Zhang, T. Zhao and N. Tsubaki, *ACS Catal.*, 2024, **14**, 17469–17479.

25 W. Tu, C. Sun, Z. Zhang, W. Liu, H. S. Malhi, W. Ma, M. Zhu and Y. F. Han, *Appl. Catal., B*, 2021, **298**, 120567.

26 M. Xu, X. Liu, G. Song, Y. Cai, B. Shi, Y. Liu, X. Ding, Z. Yang, P. Tian, C. Cao and J. J. Xu, *Catal*, 2022, **413**, 331–341.

27 H. Liu, L. Jiang, J. Khan, X. Wang, J. Xiao, H. Zhang, H. Xie, L. Li, S. Wang and L. Han, *Angew. Chem., Int. Ed.*, 2023, **135**, e202214988.

28 B. Liu, Z. Wang, T. Wei, Z. Liu and J. Li, *J. Environ. Chem. Eng.*, 2023, **11**, 110186.

29 D. Ma, Y. Xu, P. Zhai, Y. Deng, J. Xie, X. Liu and S. Wang, *Angew. Chem., Int. Ed.*, 2020, **59**, 21736–21744.

30 J. Zhu, P. Wang, X. Zhang, G. Zhang, R. Li, W. Li, T. P. Senftle, W. Liu, J. Wang, Y. Wang, A. Zhang, Q. Fu, C. Song and X. Guo, *Sci. Adv.*, 2022, **8**, eabm3629.

31 Y. Fu, C. C. Amoo, H. Qi, H. Liu, L. Zhu, P. Lu, R. Yang, C. Xing, S. Wang and J. Sun, *Chem. Eng. J.*, 2022, **438**, 135597.

32 Z. Zhang, G. Huang, X. Tang, H. Yin, J. Kang, Q. Zhang and Y. Wang, *Fuel*, 2022, **309**, 122105.

33 B. Liang, H. Duan, T. Sun, J. Ma, X. Liu, J. Xu, X. Su, Y. Huang and T. Zhang, *ACS Sustainable Chem. Eng.*, 2019, **7**, 925–932.

34 J. I. Orege, N. Liu, C. C. Amoo, J. Wei, Q. J. Ge and J. Sun, *J. Energy Chem.*, 2023, **80**, 80614–80624.

35 J. I. Orege, J. Wei, Y. Han, M. Yang, X. Sun, J. Zhang, C. C. Amoo, Q. Ge and J. Sun, *Appl. Catal., B*, 2022, **316**, 121640.

36 Z. Li, W. Wu, M. Wang, Y. Wang, X. Ma, L. Luo, Y. Chen, K. Fan, Y. Pan, H. Li and J. Zeng, *Nat. Commun.*, 2022, **13**, 2396.

37 H. Ren, H. Yang, J. Xin, C. Wu, H. Wang, J. Zhang, X. Bu, G. Yang, J. Li, Y. Sun and P. Gao, *Appl. Catal., A*, 2024, **358**, 124440.

38 Q. Yang, E. A. Fedorova, D. B. Cao, E. Saraçi, V. A. Kondratenko, C. R. Kreyenschulte, H. Lund, S. Bartling, J. Wei, D. E. Doronkin and J. D. Grunwaldt, *Nat. Catal.*, 2025, **8**, 595–606.

39 Z. Ni, X. Chen, L. Su, H. Shen, Y. Jiang, C. Feng and C. Yin, *ACS Sustainable Chem. Eng.*, 2025, **13**, 6335–6347.

40 X. Li, Z. Yang, L. Zhang, Z. He, Y. Yan, J. Ran and Z. C. Kadirova, *Fuel*, 2022, **322**, 124122.

41 H. Yang, Y. Dang, X. Cui, X. Bu, J. Li, S. Li, Y. Sun and P. Gao, *Appl. Catal., B*, 2023, **321**, 122050.

42 H. Pitayachinchot, P. Reubroycharoen, P. Prasassarakich, T. Yokoi, Y. Shen, M. Gao and C. Ngamcharussrivichai, *Environ. Technol. Innov.*, 2025, **38**, 104162.

43 H. Ma, Y. Cai, Y. Jiao, X. Liu, J. Liu, W. Guo, X. Liu, Y. Li and X. Wen, *J. Am. Chem. Soc.*, 2025, **147**, 41452–41461.

44 J. I. Orege, N. Liu, C. C. Amoo, J. Wei, Q. J. Ge and J. Sun, *J. Energy Chem.*, 2023, **80**, 80614–80624.

45 S. Z. Ghorbaei and H. A. Ebrahim, *Appl. Energy*, 2020, **277**, 115604.

46 J. Huang, S. Jiang, M. Wang, X. Wang, J. Gao and C. Song, *ACS Sustainable Chem. Eng.*, 2021, **9**, 7891–7903.

47 X. Ai, Y. Zhang, Y. Zhao, J. Hong, C. Liu and J. Li, *Fuel*, 2025, **384**, 133958.

48 D. Ma, Y. Xu, P. Zhai, Y. Deng, J. Xie, X. Liu and S. Wang, *Angew. Chem., Int. Ed.*, 2020, **59**, 21736–21744.

49 J. Han, Y. Han, J. Yu, Y. Sun, X. Cui, Q. Ge and J. Sun, *Angew. Chem., Int. Ed.*, 2025, **64**, e202420621.

50 J. Li, X. Yuan, F. Tian, M. Wang, T. Hu, G. Xiong and X. Wang, *Appl. Catal., A*, 2024, **681**, 119781.

51 M. Qing, Y. Yang, B. Wu, J. Xu, C. Zhang, P. Gao and Y. Li, *J. Catal.*, 2011, **279**, 11–22.

52 Q. Chang, J. Li, H. Suo, M. Qing, H. Wang, C. Zhang, X. Wen, H. Xiang, Y. Yang and Y. Li, *Catal. Today*, 2024, **431**, 114605.

53 Z. Yang, Z. Zhang, Y. Liu, X. Ding, J. Zhang, J. Xu and Y. Han, *Appl. Catal., B*, 2021, **285**, 119815.

54 X. Gong, Y. Liu, R. He, X. Xu, Z. Han, J. Chen, B. Feng, Z. J. Wang and A. Xing, *ChemCatChem*, 2024, **16**, e202301341.

55 K. S. Belthle, W. F. Martin and H. Tüysüz, *ChemCatChem*, 2024, **16**, e202301218.

56 H. Yu, C. Wang, X. Xin, Y. Wei, S. Li, Y. An, F. Sun, T. Lin and L. Zhong, *Nat. Commun.*, 2024, **15**, 5143.

57 Z. Cai, N. Cao, F. Zhang, X. Lv, K. Wang, Y. He, Y. Shi, H. B. Wu and P. Xie, *Appl. Catal., B*, 2023, **325**, 122310.

58 G. Song, Q. Jiang, Y. Zhai and D. Liu, *Chem. Eng. Sci.*, 2023, **280**, 119037.

59 W. Song, K. Wang, Y. Xing, W. Zhang, T. Liu, F. Bo, J. Liang, X. Gao, Q. Ma, T. Zhao and J. Zhang, *Appl. Catal., A*, 2024, **688**, 120001.

60 Q. Chang, C. Zhang, C. Liu, Y. Wei, A. V. Cheruvathur, A. I. Dugulan, J. W. Niemantsverdriet, X. Liu, Y. He, M. Qing, L. Zheng, Y. Yun and Y. Yang, *ACS Catal.*, 2018, **8**, 3304–3316.

61 G. B. Raupp and W. N. Delgass, *J. Catal.*, 1979, **58**, 348–360.

62 G. Yu, B. Sun, Y. Pei, S. Xie, S. Yan, M. Qiao, K. Fan, X. Zhang and B. Zong, *J. Am. Chem. Soc.*, 2010, **132**, 935–937.

63 Q. Yang, V. A. Kondratenko, S. A. Petrov, D. E. Doronkin, E. Saraçi, H. Lund, A. Arinchtein, R. Kraehnert, A. S. Skrypnik, A. A. Matvienko and E. V. Kondratenko, *Angew. Chem., Int. Ed.*, 2022, **61**, e202116517.

64 Q. Yang, H. Lund, S. Bartling, F. Krumeich, A. S. Skrypnik and E. V. Kondratenko, *J. Catal.*, 2023, **426**, 126–139.

65 G. P. Laan and A. A. Beenackers, *Catal. Rev.*, 1999, **41**, 255–318.

66 E. de Smit and B. M. Weckhuysen, *Chem. Soc. Rev.*, 2008, **37**, 2758–2781.

67 Y. Xu, P. Zhai, Y. Deng, J. Xie, X. Liu, S. Wang and D. Ma, *Angew. Chem., Int. Ed.*, 2020, **59**, 21736–21744.

68 B. Liu, S. Geng, J. Zheng, X. Jia, F. Jiang and X. Liu, *ChemCatChem*, 2018, **10**, 4718–4732.

69 R. Ye, J. Ding, T. R. Reina, M. S. Duyar, H. Li, W. Luo, R. Zhang, M. Fan, G. Feng, J. Sun and J. Liu, *Nat. Synth.*, 2025, **4**, 288–302.

70 M. K. Khan, P. Butolia, H. Jo, M. Irshad, D. Han, K. W. Nam and J. Kim, *ACS Catal.*, 2020, **10**, 10325–10338.

71 Q. Xu, X. Xu, G. Fan, L. Yang and F. Li, *J. Catal.*, 2021, **400**, 355–366.